STE-QUEST - Test of the Universality of Free Fall Using Cold Atom Interferometry

D. Aguilera[1], H. Ahlers[2], B. Battelier[3], A. Bawamia[4],
A. Bertoldi[3], R. Bondarescu[5], K. Bongs[6], P. Bouyer[3],
C. Braxmaier[1,7], L. Cacciapuoti[8], C. Chaloner[9], M. Chwalla[10],
W. Ertmer[2], M. Franz[11], N. Gaaloul[2], M. Gehler[8],
D. Gerardi[10], L. Gesa[12], N. Gürlebeck[7], J. Hartwig[2],
M. Hauth[13], O. Hellmig[14], W. Herr[2], S. Herrmann[7], A. Heske[8],
A. Hinton[6], P. Ireland[9], P. Jetzer[5], U. Johann[10], M. Krutzik[13],
A. Kubelka[7] C. Lämmerzahl[7], A. Landragin[15], I. Lloro[12],
D. Massonnet[16], I. Mateos[12], A. Milke[7], M. Nofrarias[12],
M. Oswald[11], A. Peters[13], K. Posso-Trujillo[2], E. Rasel[2],
E. Rocco[6], A. Roura[17], J. Rudolph[2], W. Schleich[17],
C. Schubert[2], T. Schuldt[1,11], S. Seidel[2], K. Sengstock[14],
C. F. Sopuerta[12], F. Sorrentino[18], D. Summers[9], G. M. Tino[18],
C. Trenkel[19], N. Uzunoglu[20], W. von Klitzing[21], R. Walser[22],
T. Wendrich[2], A. Wenzlawski[14], P. Weßels[23], A. Wicht[4],
E. Wille[8], M. Williams[19], P. Windpassinger[14], N. Zahzam[24]

[1] German Aerospace Center (DLR), Institute for Space Systems,
Robert-Hooke-Str. 7, 28359 Bremen, Germany
[2] Institute of Quantum Optics, Leibniz University Hanover, Welfengarten 1, 30167
Hanover, Germany
[3] Laboratoire Photonique, Numérique et Nanosciences-LP2N Université
Bordeaux-IOGS-CNRS: UMR 5298, Talence, France
[4] Ferdinand-Braun-Institut, Gustav-Kirchhoff-Str. 4, 12489 Berlin, Germany
[5] Institute of Theoretical Physics, University of Zurich, Winterthurerstr. 190, 8057
Zurich, Switzerland
[6] School of Physics and Astronomy, University of Birmingham, Birmingham, B15
2TT, United Kingdom
[7] Center of Applied Space Technology and Microgravity (ZARM), University
Bremen, Am Fallturm, 28359 Bremen, Germany
[8] ESA - European Space Agency, ESTEC, Keplerlaan 1, 2200 AG Noordwijk ZH,
Netherlands
[9] SEA House, Bristol Business Park, Coldharbour Lane, Bristol BS16 1EJ, United
Kingdom
[10] Astrium GmbH - Satellites, Claude-Dornier-Str., 88090 Immenstaad, Germany
[11] Institute of Optical Systems, University of Applied Sciences Konstanz (HTWG),
Brauneggerstr. 55, 78462 Konstanz, Germany
[12] Institut de Ciències de l'Espai (CSIC-IEEC), Campus UAB, Facultat de Ciències,
08193 Bellaterra, Spain
[13] Humboldt-University Berlin, Institute for Physics, Newtonstr. 15, 12489 Berlin,

Germany

[14] Institute of Laser-Physics, University of Hamburg, Luruper Chaussee 149, 22761 Hamburg, Germany

[15] SYRTE- Observatoire de Paris, 61 avenue de l'obsevatoire, 75014 Paris, France

[16] CNES - Centre national d'etudes spatiales, 2 place Maurice Quentin, 75039 PARIS CEDEX 01, France

[17] Department of Quantum Physics, University of Ulm, Albert-Einstein-Allee 11, 89081 Ulm, Germany

[18] Dipartimento di Fisica e Astronomia and LENS Laboratory, Università di Firenze - INFN, Sezione di Firenze - via G. Sansone 1, 50019 Sesto Fiorentino (Firenze), Italy

[19] Astrium Ltd, Gunnels Wood Road, Stevenage SGI 2AS, United Kingdom

[20] National Technical University of Athens, 28 Oktovrio 42, 10682 Athens, Greece

[21] Institute of Electronic Structure and Laser, Foundation for Research and Technology - Hellas, P.O. Box 1527, 6R-71110 Heraklion, Greece

[22] Institut für Angewandte Physik, Technische Universität Darmstadt, Hochschulstr. 4a, 64289 Darmstadt, Germany

[23] LZH - Laser Zentrum Hannover e.V., Hollerithallee 8, 30419 Hannover, Germany

[24] ONERA - Office National d'Etude et de Recherches Aerospatiales, Chemin de la Huniere, 91761 Palaiseau, France

E-mail: `gaaloul@iqo.uni-hannover.de`, `norman.guerlebeck@zarm.uni-bremen.de`, `thilo.schuldt@dlr.de`

Abstract. The theory of general relativity describes macroscopic phenomena driven by the influence of gravity while quantum mechanics brilliantly accounts for microscopic effects. Despite their tremendous individual success, a complete unification of fundamental interactions is missing and remains one of the most challenging and important quests in modern theoretical physics. The STE-QUEST satellite mission, proposed as a medium-size mission within the Cosmic Vision program of the European Space Agency (ESA), aims for testing general relativity with high precision in two experiments by performing a measurement of the gravitational redshift of the Sun and the Moon by comparing terrestrial clocks, and by performing a test of the Universality of Free Fall of matter waves in the gravitational field of Earth comparing the trajectory of two Bose-Einstein condensates of ^{85}Rb and ^{87}Rb. The two ultracold atom clouds are monitored very precisely thanks to techniques of atom interferometry. This allows to reach down to an uncertainty in the Eötvös parameter of at least $2 \cdot 10^{-15}$. In this paper, we report about the results of the phase A mission study of the atom interferometer instrument covering the description of the main payload elements, the atomic source concept, and the systematic error sources.

1. Introduction

The current theory of gravity, general relativity, is based on Einstein's Equivalence Principle. It consists of three parts: The Universality of Free Fall (UFF), the Local Position Invariance, and the Local Lorentz Invariance.

The Universality of Free Fall (UFF),‡ implies that the trajectories of test masses, for which tidal deformations, self-gravity, electromagnetic charges, spin, etc. are negligible, depend only on their initial position and their initial velocity. The Local Lorentz Invariance postulates that the the outcome of any non-gravitational experiment performed in a freely falling frame is independent of the velocity and of the orientation of that frame. The Local Position Invariance states that the outcome of such an experiment is also independent of where and when in the universe it is carried out, cf. [1, 2, 3].

Essentially all efforts to unify gravity with the other fundamental interactions (e.g. string theory, canonical quantum gravity, etc.) predict a violation of Einstein's Equivalence Principle at some scale [2, 4]. Therefore, a crucial step towards an unified theory requires experiments that test the assumptions and principles of general relativity and search for possible violations or set bounds to the possible deviations. Such deviations and also their absence could, indeed, shed some light on the quantum nature of gravity. This holds in particular for the low energy limits of string theory, where extra moduli fields arise, see, e.g., [5, 6, 7]. Moreover, theories with a fifth force, theories invoked to explain dark energy, and theories with varying fundamental constants and non-minimal coupling can entail a violation of the UFF, see, e.g., [8, 9], [10, 11, 12], and [13, 14, 15], respectively. Phenomenological frameworks describing a violation of the UFF are, for example, the PPN formalism and the Standard Model Extension, see, e.g., [16, 17]. A violation of the UFF is quantified by the Eötvös ratio $\eta = |\Delta a|/|\vec{g} \cdot \vec{e}_{\Delta a}|$, where Δa denotes the differential acceleration of the two test bodies and $\vec{g} \cdot \vec{e}_{\Delta a}$ the projection of the local gravitational acceleration $\vec{g}$ onto the sensitive axis $\vec{e}_{\Delta a}$ of the accelerometer.

STE-QUEST (Spacetime Explorer and Quantum Equivalence Principle Space Test) is a medium-size (M3) candidate satellite mission, which we proposed to ESA in the scope of the Cosmic Vision program. It is currently in the assessment phase (Phase A). The planned STE-QUEST satellite consists of a dual species (^{85}Rb and ^{87}Rb) atom interferometer (AI) and a microwave link. A microwave clock based on laser cooled Caesium atoms and an optical link are considered as an optional payload. The AI shall test UFF with quantum matter waves, i.e. Bose-Einstein condensates (BEC) to the unprecedented accuracy of about $\eta \leq 2 \cdot 10^{-15}$. The microwave link will allow for a measurement of the gravitational redshift due to the Sun's and the Moon's gravitational potential by ground clock comparison, expected to reach an uncertainty of $5 \cdot 10^{-7}$ and $9 \cdot 10^{-5}$, respectively. The former is presently measured to the few percent level [18, 19]; the latter is not experimentally determined yet. In case the optional atomic Caesium clock is included in the STE-QUEST payload, the redshift due to the Earth's

‡ The UFF is also called Weak Equivalence Principle.

gravitational field will also be measured with an uncertainty of $2 \cdot 10^{-7}$ resulting in a factor 350 improvement over the current best measurements by Gravity Probe A [20]. The long common-view contacts required to compare ground clocks and the need for a strong gravity field for maximizing an eventual UFF-violating signal define the highly elliptic STE-QUEST orbit. The mission details were investigated in an independent industry study; its results are presented in [21]. Preliminary aspects of the mission were presented in a recent conference proceedings [22].

Apparatus	Target precision for η	Species	Ref.
Torsion balance[3]	$(0.3 \pm 1.8) \cdot 10^{-13}$	Ti, Be	[23]
Lunar Laser Ranging[2,3]	$(-0.8 \pm 1.8) \cdot 10^{-13}$	Moon, Earth	[24]
AI/FG5	$(7 \pm 7) \cdot 10^{-9}$	Cs, Glass	[25]
Dual AI (Garching)	$(1.2 \pm 1.7) \cdot 10^{-7}$	^{85}Rb, ^{87}Rb	[26]
Dual AI (ONERA)	$(1.2 \pm 3.2) \cdot 10^{-7}$	^{85}Rb, ^{87}Rb	[27]
Dual AI (Firenze)	$7 \cdot 10^{-7}$	^{87}Sr, ^{88}Sr	[28]
Dual AI[1] (Hanover)	10^{-9}	^{85}Rb, K	[29]
Dual AI[1] (Berkeley)	10^{-14}	^{6}Li, ^{7}Li	[30]
Dual AI tower initial/upgrade[1] (Stanford)	$10^{-15}/10^{-16}$	^{85}Rb, ^{87}Rb	[31]

Table 1. Existing and planned UFF tests on ground. 1) Work in progress. 2) LLR references the differential acceleration between Moon and Earth to the gravitational field of the Sun. All other tests in this table are referenced to the gravitational field of Earth. 3) Macroscopic test masses.

Apparatus	Target precision for η	Species	Ref.
SAI ground based/in zero-g	$[10^{-7}/1.8 \cdot 10^{-10}]$ [2]	^{87}Rb	[32]
ICE	10^{-11}	^{87}Rb, K	[33]
QUANTUS	$6.3 \cdot 10^{-11}$	^{87}Rb, K	[34]
μ-scope[1]	10^{-15}	Pt, Ti	[35]
STEP[1]	10^{-18}	Pt, Ir, Nb, Be	[36]
GG[1]	10^{-17}	[3]	[37]

Table 2. Planned and proposed UFF tests in space and zero-g environments. All tests in this table are referenced to the gravitational field of Earth. 1) Macroscopic test masses. 2) Single species experiment, sensitivity given in $\mathrm{m\,s^{-2}\,Hz^{-1/2}}$. 3) Not yet decided.

Many tests of the UFF on ground and in micro-gravity environments reported no violation down to the $1 \cdot 10^{-13}$ level; we summarized them in Tab. 1 and Tab. 2. STE-QUEST performs a *quantum* test of the UFF by tracking the propagation of matter waves in Earth's gravitational field by means of a two species atom interferometer achieving an accuracy of at least $2 \cdot 10^{-15}$. The matter waves are generated from two

ensembles of Rubidium isotopes (^{85}Rb and ^{87}Rb), which are cooled down until Bose-Einstein condensation sets in, allowing an improvement of the UFF test by orders of magnitude compared to the non-condensate matter case, see [26]. The interferometer is based on previous studies like SAI (Space Atom Interferometer) [32], SpaceBEC (Quantum gases in microgravity), the french CNES project I.C.E. (Interférométrie Cohérente pour l'Espace) [33] as well as the German DLR funded projects QUANTUS (Quantengase unter Schwerlosigkeit) and PRIMUS (Präzisionsinterferometrie unter Schwerelosigkeit). Within QUANTUS interferometry was already demonstrated with degenerate ^{87}Rb atoms under microgravity in the drop tower at ZARM (Germany) [38] and aims with the MAIUS experiments at realizing quantum gases interferometry on sounding rockets starting from 2014.

An advantage of using matter waves is that the center of mass positions of the BECs can be measured independently for each wave packet and be brought to coincide. This assumption in the UFF can never be fully matched using classical bulk matter. At best the deviation caused by initially different positions can be simulated. The experiment proposed here constitutes also a test of the motion of two superposed center of masses. Thus, it can be interpreted as a test of classical general relativity coupled to a Klein-Gordon field in a non-relativistic limit or, equivalently, the Schrödinger-Newton equation with an external gravitational potential, see [39].

The paper is organized as follows: In the next Section, the mission concept and the expected performance of the AI are outlined. In Sec. 3, the principle experimental set up is described. The requirements necessary to achieve the expected accuracy of $2 \cdot 10^{-15}$ for the Eötvös ratio and the error sources are discussed in Sec. 4. The planned payload for the STE-QUEST mission is detailed in Sec. 5.

2. Objectives, Performance and Operation

The objective of the STE-QUEST atom interferometer is to test the UFF using matter waves to an uncertainty in the Eötvös parameter better than $2 \cdot 10^{-15}$ [40]. For STE-QUEST, $\Delta a = a_{87} - a_{85}$ denotes the differential acceleration between the two wave packets, the sensitivity axis $\vec{e}_{\Delta a}$ is given by the effective wave vector of the beam splitting light fields $\vec{k} \parallel \vec{e}_{\Delta a}$. A high common mode rejection ratio for the differential acceleration of $\approx 2.5 \cdot 10^{-9}$ is a driving requirement for the overall performance. This and the heritage from various precision and mixture experiments motivated the choice of ^{87}Rb and ^{85}Rb as atomic species for STE-QUEST. Following [7], which is one candidate theory describing violations of the UFF, one would expect an approximately 10–30 times larger violation of the UFF for other choices of isotopes like ^{87}Rb and K. However, for these the common mode rejection rejection ratio would be ≈ 300 for a vibrational background acceleration comparable to STE-QUEST [33]. Thus, although the violation might be smaller the better common mode rejection for the choice of $^{85/87}$Rb counter-balances this effectively turning it into the superior choice. Compared to state of the art torsion balance [23] and LLR tests [24] as well as planned or proposed satellite
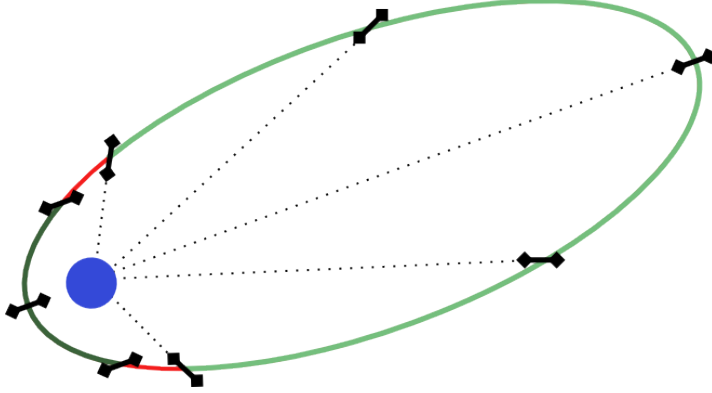
Figure 1. Highly elliptical orbit chosen for STE-QUEST clock comparisons [40]. During perigee pass (dark green) of the 16 h per revolution, the spacecraft will be inertially pointing for 0.5 h allowing for testing the UFF with the AI part of the payload. After the perigee phase, the spacecraft orientation is changed to nadir pointing (red) for clock measurements during the apogee phase (light green). In parallel, AI parameters are verified and calibrated. The orientation of the atom interferometer sensitive axis is also indicated in black.

missions [35, 36, 37] with macroscopic test masses, STE-QUEST offers a complementary approach as a test with a quantum sensor. Several advantages over proposed ground based atom interferometer experiments [31, 41, 42] are present due to the "free fall" conditions in a space borne apparatus. Here, the center of mass of the atoms is at rest with respect to the experimental set-up. Consequently, long free evolution times $2T = 10\,\mathrm{s}$ can be realised in a compact set-up. This is a key ingredient to reach a high sensitivity to accelerations $\vec{a}$, because the phase shift in the interferometer scales as $\phi_{acc} = \vec{k} \cdot \vec{a} T^2$ with the wave number k. For ground based experiments, suspension techniques [30] or large momentum beam splitters [31, 41, 42] are proposed to reach high scaling factors although additional constraints due to systematic errors have to be expected [43]. Moreover, the low background accelerations of $4 \cdot 10^{-7}\,\mathrm{m\,s^{-2}}$ in STE-QUEST compared to $9.8\,\mathrm{m\,s^{-2}}$ on ground reduce systematic effects and enable the use of weak traps during the preparation of the atomic ensembles. This is mandatory to reach atom numbers of 10^6 in dilute ensembles and to efficiently apply delta kick cooling techniques [44, 45, 46, 38] to reach low expansion rates. Furthermore, a symmetric beam splitting technique [47] can be implemented which inherently suppresses systematic errors and associated noise sources. An additional distinctive advantage is the satellite motion which causes a modulation of a possible violation signal and allows for null measurements. Systematic error which are stable in time and do not depend on the Earth's gravity field can thus be estimated and ruled out.

In STE-QUEST, a quantum projection noise limited sensitivity per cycle of $\sigma_{\Delta a}/\sqrt{T_c} \approx 3 \cdot 10^{-12}\,\mathrm{m\,s^{-2}}$ for 10^6 atoms of each species, a wave number $k = 8\pi/(780\,\mathrm{nm})$, a free evolution time $T = 5\,\mathrm{s}$, and a cycle time $T_c = 20\,\mathrm{s}$ is anticipated. This value assumes a contrast $C = 0.6$. It is affected by a dephasing due to Earth's gravity gradient T_{gg} coupled to the initial size σ_r and expansion rate σ_v of the atomic ensembles and is

estimated by the formula $C = \exp\{-(k\sigma_r T_{gg} T^2)^2/2\} \cdot \exp\{-(k\sigma_v T_{gg} T^3)^2/2\}$ [48].

The STE-QUEST AI will measure for $0.5\,\text{h}$ during each perigee pass of the highly elliptical orbit with a total duration of $16\,\text{h}$ (see Fig. 1). At perigee, the proximity to Earth maximizes the signal of an eventual UFF-violating signal. The satellite will be non-rotating during this phase which leads to a varying projection of the local gravitational acceleration g and of the gravity gradient T_{gg} onto the sensitive axis. Additionally, the interferometer contrast increases as the projection decreases. The altitude at perigee increases periodically during the mission from about $700\,\text{km}$ to $2200\,\text{km}$ and then decreases back to $700\,\text{km}$. An integrated sensitivity per revolution to the Eötvös ratio of $\sigma_\eta^{1\,\text{rev}} \approx 5 - 5.2 \cdot 10^{-14}$ is expected when taking into account the shot noise limit, altitude, and attitude of the satellite with respect to Earth.

Therefore, an integration time of about $1.5\,\text{years}$ is required to reach the target sensitivity of $\sigma_\eta^{625\,\text{revs}} \approx 2 \cdot 10^{-15}$ compatible with a total mission duration of $5\,\text{years}$. Calibration procedures will be carried out in the apogee phase. Byproduct of the mission will be the most extended evolution time of cold atoms in a free fall experiment.

3. System

3.1. Atom Source

In order to reach the target performance, a Bose-Bose mixture of 10^6 atoms of each of the isotopes must be prepared in $10\,\text{s}$ maximum. To this end, an atom chip [49, 50, 51] setup is used allowing for a fast evaporation and a low power consumption necessary for a satellite-borne device. Moreover, we opt for the use of quantum degenerate ensembles for several reasons. The most important are (i) keeping a reasonably small size of the mixture after a free evolution time of $10\,\text{s}$, (ii) reducing the size-related-systematics to an acceptable level and (iii) profiting from the additional control offered by a tunable interactions input state of the atom interferometer. It is important to notice that the dephasing associated to mean-field effects in atom interferometers with interacting sources is reduced here by letting the atomic clouds freely expand until they reach the linear regime of interactions [52]. Only at this point, the interferometry sequence is started.

The source generation sequence depicted in Fig. 2 is initiated by loading an ultra-high vacuum (UHV) 3D-MOT from a high vacuum (HV) 2D$^+$-MOT through a differential pumping stage [53, 34] as illustrated in Fig. 3. The HV environment is intended for the atomic source, which operates at a Rubidium vapor pressure of a few $10^{-7}\,\text{mbar}$. This is the optimal vapor pressure range for the 2D$^+$-MOT that provides a pre-cooled beam of atoms towards the UHV chamber. Since the 2D$^+$-MOT gains an additional cooling mechanism through the means of two unbalanced counter propagating laser beams along the atom's trajectory, the velocity and the velocity spread of the atoms can be controlled and fast loading ($2\,\text{s}$ at a flux of 10^{10} ^{87}Rb atoms per second) into the 3D-MOT can be achieved. Thanks to the natural abundance of the ^{85}Rb isotope
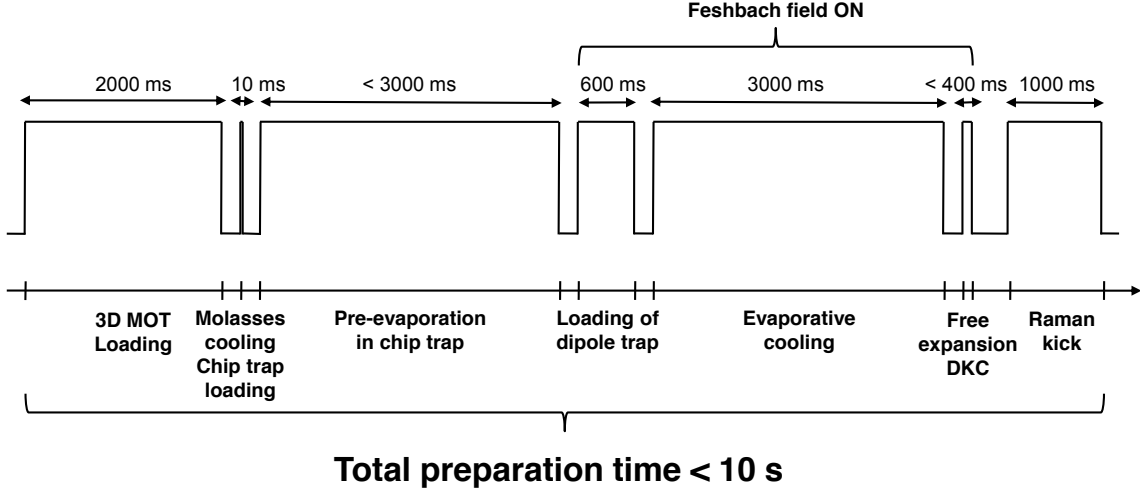
Figure 2. BEC generation and preparation sequence. The cycle starts with a loading phase of the main chamber by a 2D+-MOT. In a rather short time the atoms are trapped in the chip magnetic trap. This allows to pre-evaporate the dual source for 3 s using RF fields. When the intra-species attractive collisions in ^{85}Rb start to be severe due to the increased density of the gas, the Feshbach magnetic field is ramped up tuning these collisions to repulsive. The crossed-beam dipole trap is then loaded and the evaporation is performed by lowering the power of the tow laser beams. When the two gases reach degeneracy, they are released and freely expand. As soon as the linear regime of interactions is reached, a delta-kick cooling pulse is applied and the Feshbach field is switched-off. The two mixed clouds are pushed away from the chip surface by applying a Raman pulse normal to it. The same Raman beam is used to stop the atomic clouds when they reach a distance of about 15 mm from the surface avoiding the diffraction of the interferometry beams on it. This preparation phase is lasting less than 10 s in agreement with the science objectives.

($\geq 72\%$) and the fact that two to three orders of magnitude less ^{85}Rb atoms (compared to ^{85}Rb) are necessary at the MOT stage, the same source will also be able to generate the envisioned flux of 10^9 ^{85}Rb atoms per second.

A multi-layer atom chip setup (Fig. 3) is used to trap the atoms from the atomic beam. In cooperation with external magnetic bias fields, the chip structures can generate a variety of trap configurations – from very shallow traps to collect the initial MOT to very tight confinement for fast evaporation [54]. Initially, the largest available (mesoscopic) chip structures are used for the 3D-MOT. For each species, three pairs of counter propagating laser beams, intersecting at the field minimum, are used to generate a mirror MOT [55]. The beams contain cooling and repumping light for $^{87/85}$Rb as well. Accordingly, more than 10^{10} ^{87}Rb atoms and 10^9 ^{85}Rb atoms can be captured in a total loading time of 2 seconds.

Once the atoms are captured in the chip MOT, the magnetic fields are switched-off for a few milliseconds (5 ms)to further cool the atoms through polarization gradient cooling . The final temperatures of the clouds after all laser cooling steps will be as
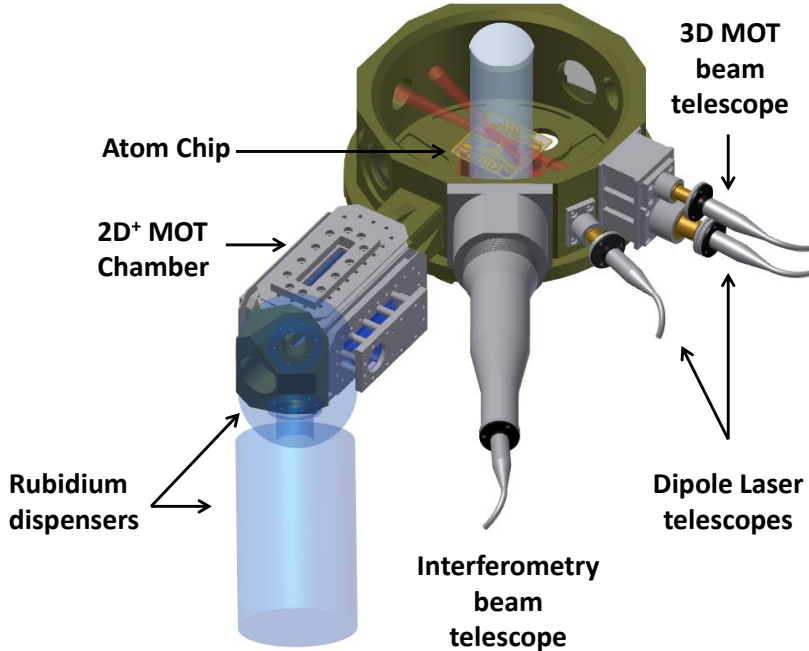
Figure 3. Vacuum chambers and main laser beams. A beam of pre-cooled atoms, initially released from the two isotopes reservoirs (light blue), is pushed from the 2D$^+$-MOT to the main science chamber via a differential pumping stage. A MOT is loaded right above the center of the atom chip and the atoms are pre-evaporated, after being loaded in the chip trap, using the chip RF antenna. The dipole lasers are depicted by the crossed red beams which trap the atoms at the chip vicinity to finalize the evaporation process. Once the two BECs are obtained, the interferometry pulses are applied by a couple of Raman beams (large light blue beam) along the sensitive axis.

low as 20μK. After switching-on the offset magnetic field ($5\,$ms), the $^{87/85}$Rb atoms can be optically pumped to the weak-field seeking states $|F = 2, m_F = 2 >_{87}$ and $|F = 3, m_F = 3 >_{85}$ in a fraction of a millisecond.

After state preparation, the lasers are switched-off and the atoms are trapped solely by magnetic fields in a Ioffe-Pritchard trap created by the chip. One exquisite feature of this technology is the ability to generate quite shallow traps (geometric mean of about 7 Hz) being in the same time rather deep (around $100\,\mu$K trap depth in the 3 space directions). In this fashion, the atom loss during the MOT trapping is negligible. The temperatures, however, will rise because of heating and adiabatic compression of the trap.

A pre-cooling step is necessary to gain a sufficiently large phase space density (PSD of 10^{-4}-10^{-5}) before starting the all-optical evaporation. Radio frequency (RF)

radiations are used to pre-evaporate ^{87}Rb atoms solely. The number of ^{85}Rb atoms remains approximately constant during this pre-cooling step thanks to the isotope selectivity of these radiations. The ^{85}Rb atoms cool down sympathetically through collisions with ^{87}Rb and rethermalize constantly. In about 3 s a temperature of a few μK and a size of about $10 \, \mu$m are reached allowing to match the tight confinement of the optical trap and ensure efficient transfer. While the PSD is increased by an order of magnitude, the temperature rises due to an increase in inelastic collisions, especially for ^{85}Rb atoms. This leads to a loss of one order of magnitude in atom numbers leaving the two ensemble with 10^9 atoms for ^{87}Rb and 10^8 for ^{85}Rb left at this step. No further cooling is possible since the 3-body losses of ^{85}Rb due to its negative scattering length start to be severe at high densities.

Loading the optical trap is costing only another order of magnitude in particles number thanks to the size-compressed and pre-cooled samples. This loading is performed after ramping up a Feshbach field of about 158 G in 300 ms to avoid disturbing and heating the atoms with eddy currents. This field drives the ^{85}Rb atoms to a region of positive scattering lengths (ranging from $500 \, a_0$ to $900 \, a_0$) to allow for an efficient evaporation [56, 57]. Moreover, the magnetic field can be used to change the ratio between elastic and inelastic collisions in ^{85}Rb and thereby minimize losses by two- and three-body collisions. For all the range of values of the scattering lengths of ^{85}Rb mentioned above, the two degenerate gases should be in a miscible phase [56]. The two ensembles are loaded in a first dipole beam in 300 ms followed by a second one with a switch-on duration comparable to the first. Once in place, the final evaporation is carried out. The phase transition to Bose-Einstein condensation (BEC) can be reached in $2-3$ s using runaway all-optical evaporation [58]. When 10^6 atoms are obtained in the condensed phase for each isotope the far-off resonance lasers are turned-off in 50 ms.

An optimization step is starting at this point and lasts for less than 400 ms alternating free expansion and delta-kick cooling (DKC) pulse(s)[52]. A free expansion of the atomic clouds is starting in the Feshbach field. This expansion phase serves to damp down the density of ^{85}Rb to a level where the ensemble is stable even in the absence of an external magnetic field [52]. Not more than a few ms $(3-6)$ are needed to this end. Nevertheless, the bias field is kept for about 10 ms after condensation in order to allow the two ensembles to reach the linear regime of interactions and avoid mean-field effects during interferometry. A DKC brief pulse(s) (a fraction of a ms) absorb(s) most of the kinetic energy of the atoms [44, 45, 46, 38]. This is achieved by suddenly turning -on and -off the final crossed laser traps acting as an atomic lens collimating the BEC clouds to a temperature equivalent expansion of 70 pK. This very low effective temperature accessible with DKC is necessary for keeping the size-related systematics at a low level after 10 s avoiding fringe pattern to build up. An alternative to this low expansion rate is to recover the contrast by unbalancing the time intervals between the interferometry pulses in a suitable way [59].

Since the last value of the magnetic field tunes solely the scattering length of ^{85}Rb, it is possible to optimize its magnitude to reject common size-related error sources such

as wave-front curvatures [52]. This reduces the need for interferometry mirrors from extremely good quality ($\lambda/300$) to values of about $\lambda/30$. At this point the Feshbach field is switched-off without any influence on the free expansion of ^{85}Rb which recovers its negative scattering length of $-445\,a_0$.

A last manipulation before the interferometry first pulse consists in driving a Raman transition for the atoms in each cloud. One beam normal to the chip and its reflection from the surface are responsible for the 2-photon transition. As a result the atoms travel away from the chip surface. This serves to avoid wave front errors due to the diffraction of the interferometry beams on the chip. In a time interval of 1 s, the two ensembles are stopped by reversing the beams at a safe distance of about 15 mm.

3.2. Interferometery Scheme

The interferometer scheme, detailed in [60], is based on a Mach-Zehnder like atom interferometer employing two photon Raman-transitions in a double diffraction setup for the coherent manipulation [47]. The interferometric sequence in this case is composed of a coherent splitting of the wave function into the two interferometer states, a mirroring of theses states after a given interferometer time T and another subsequent splitting after a time T which closes the interferometer and encodes the phase difference between both paths into the population of the output ports. A two photon Raman-transition couples the two hyperfine levels of the rubidium ground state while at the same time transferring a momentum of $2\hbar k_s$ to the atoms, where $\hbar k_s$ denotes the momentum transfer corresponding to the single photon transition. If the initial state has a vanishing momentum in comparison to the two-photon light field, the two momentum states with $\pm 2\hbar k_s$ are degenerated and a splitting into both states will occur as long as the effective momentum transfer is geometrically possible. This is obtained by retro-reflecting the light fields to driving the Raman-transitions. In this scheme, an effective momentum splitting of $4\hbar k_s = \hbar k$ is realised while the hyperfine state in the trajectories is always the same. The higher order coupling of the light fields yields to a stronger dependence of the transition probability on the velocity spread of the atomic cloud. Therefore as described in [52] an atomic ensemble with an effective temperature of 70 pK is used as initial interferometer state. Residual occupation of the state $0\hbar k_s$ is removed via a resonant light field since the internal state is different to the diffracted orders with $\pm 2\hbar k_s$. A sketch of the interferometric sequence can be seen in Fig. 4. Using a double diffraction scheme reduces the impact of phase shifts dependent on the hyperfine state. Examples are magnetic fields and off-resonant light fields coupling into the interferometer. Magnetic field gradients can still give rise to a residual phase shift. To circumvent this effect, the input hyperfine state can be switched between two successive measurements leading to a reversal of the effective coupling to magnet fields and thus suppressing gradient dependent phase shifts.
Gravimetric measurements based on atom interferometers are usually limited by environmental noise, mainly vibrations of the experimental platform. The impact of
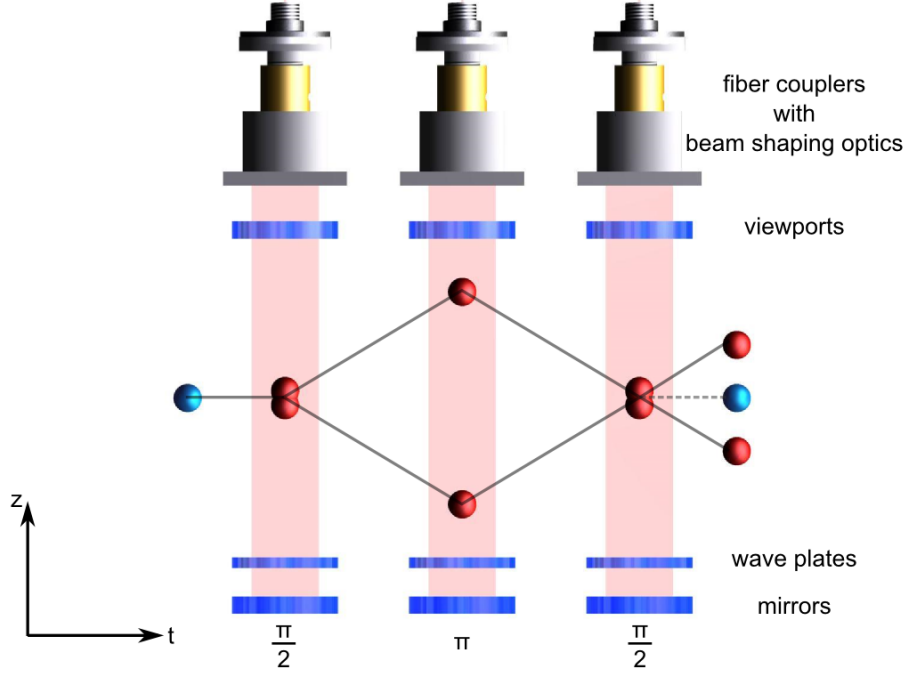
Figure 4. Interferometer scheme in a time series. The sequentially applied laser pulses split, reflect, and recombine the atomic wave-functions. The colour of the balls represent the two hyperfine levels of the rubidium atoms. After release, the atoms are in the excited state (red balls), and during the atom interferometry sequence in the ground state (red circles). In this sketch perfect beam-splitting efficiency is assumed.

these accelerations on the interferometer phase is determined by the sensitivity function which is dependent on the effective wave vector k, the pulse timings and the Rabi-frequency of the two photon transition [61]. As long as these values are matched, environmental noise would lead to the same phase shifts for both species and thus vanish in the differential signal. The interferometer time T and beam splitter pulse duration is set to be equal due to the use of common switching elements for all beams. To match the effective wave vectors and the Rabi-frequencies, the detuning of the Raman-beams to the single photon excitation and the power of the individual beams can be adjusted. The quality of this match directly influences the possible suppression of common mode accelerations (see Sec. 4) and is discussed in more detail in [60].

4. Error budget

The choice of ^{87}Rb and ^{85}Rb is specifically attributed to the engineering of a large common mode rejection ratio. Still, several effects acting differently on the two isotopes can lead to a differential acceleration signal masking a possible violation signal. Additionally, every random fluctuation of a bias term has to stay below shot noise to not impede the targeted uncertainty. A detailed discussion can be found in [60].

Noise source	Conditions	Limit $(10^{-12}\,\mathrm{m\,s^{-2}})$
Shot noise	10^6 atoms, $C = 0.6$	2.93
Linear vibrations	Suppression ratio $2.5 \cdot 10^{-9}$	≈ 1
Beam splitter laser linewidth	Linewidth $100\,\mathrm{kHz}$	0.8
Magnetic fields	$B_0 = 1\,\mathrm{mG}$, $\nabla B_0 = 83\,\mu\mathrm{G\,m^{-1}}$	0.11
Mean field	Beam splitting accuracy 0.001, 20 % fluctuation in N_{87}/N_{85}	0.3
Overlap	10 % fluctuation per cycle	< 0.1
Sum		3.2

Table 3. Preliminary assessment of statistical errors for the STE-QUEST AI

Shot noise and contrast Both atomic ensembles will feature $N = 10^6$ atoms. The effective wave vector of $k = 8\pi/(780\,\mathrm{nm})$, the free evolution time $T = 5\,\mathrm{s}$, and the contrast $C = 0.6$ are linked to the shot noise limited sensitivity per cycle $\sigma_{\Delta a}/\sqrt{T_c} = \sqrt{2/N}\,(CkT^2)^{-1} \approx 2.93 \cdot 10^{-12}\,\mathrm{m\,s^{-2}}$ for a cycle time $T_c = 20\,\mathrm{s}$. Herein, the contrast is limited by velocity dependent phase shift in the interferometer coupled to the velocity distribution of the atomic ensemble [62, 48]. The dominant contribution is given by Earth's gravity gradient T_{gg}. Since the orientation and altitude of the satellite with respect to the Earth changes during perigee pass so does the contrast. Here, $C = 0.6$ is the minimum for an altitude of $700\,\mathrm{km}$ above Earth and $\vec{k} \parallel \vec{g}$. The rotation rates of $10^{-6}\,\mathrm{rad/s}$ in all three axes do not significantly affect the contrast in STE-QUEST. Velocity selectivity of the beam splitter neither threatens the contrast.

Spurious accelerations of the spacecraft Any bias acceleration or vibration is suppressed in the differential signal. Suppression ratios of $140\,\mathrm{dB}$ were demonstrated in single species differential atom interferometers [63]. This cannot directly be transferred to the dual species case, but the response of an atom interferometer to perturbations is well understood [61, 33]. Thus, the case of STE-QUEST can be modeled and from matching the wave vectors of the two species to 10^{-9} and the Rabi frequencies to 10^{-4} a suppression ratio of $2.5 \cdot 10^{-9}$ can be obtained. This assumes the same switching element for both isotopes inherently matching the pulse duration and free evolution times.

Beam splitter laser linewidth During the beam splitting process, one of the two light fields driving the Raman transition is reflected at the retro reflection mirror while the other is not. Consequently, a time delay between the arrival of the two phase locked laser beams results. This implies a sensitivity to frequency jitter of the beam splitter lasers during the time delay [64]. For a Lorentzian linewidth of $100\,\mathrm{kHz}$ integrated over the beam splitter pulse duration ($100\,\mu\mathrm{s}$) the noise contribution per shot is estimated

to $8 \cdot 10^{-13}\,\mathrm{m\,s^{-2}}$, well below the STE-QUEST requirements.

Gravity gradients and rotations, photon recoil In addition to the leading phase term $\propto kT^2$ several other phase terms arise due to spurious rotation rates of $10^{-6}\,\mathrm{rad/s}$ in all three axes and Earth's gravity gradient of $T_{gg} \leq 2.5 \cdot 10^{-6}\,\mathrm{s^{-2}}$ as derived in [42, 65]. Most of these terms vanish due to the common mode suppression ratio, but those proportional to differential position and differential velocity of the atoms remain. The center of mass overlap at the first beam splitter pulse has to be better than $1.1\,\mathrm{nm}$ and $0.31\,\mathrm{nm\,s^{-1}}$ in all three directions. This implies restrictions on the magnetic field gradients during preparation which have to be below $3\,\mu\mathrm{G\,m^{-1}}$. The differential displacement in the optical trap with a trapping frequency of $42\,\mathrm{Hz}$ stays within the defined limit on relative spatial displacement for the gravity gradient of $T_{gg} = 2.2 \cdot 10^{-6}\,\mathrm{s^{-2}}$, and for rotation rates below $1.4\,\mathrm{mrad/s}$ imposing a Coriolis force coupled with the distance to the center of mass of the satellite defensively assumed to be $2\,\mathrm{m}$, magnetic field gradients below $12\,\mu\mathrm{G\,m^{-1}}$, and bias accelerations below $20\,\mu\mathrm{m\,s^{-2}}$. This is compatible with operation both during inertially and nadir pointing phases. Contributions to the differential acceleration signal due to payload and spacecraft self-gravity will be subtracted by comparing perigee and apogee measurements. In first order, the gravity gradients are dominated by the Earth's contribution.

Magnetic fields During interferometry, both isotopes are in the magnetic substate $m_f = 0$ to exclude a linear Zeeman shift. Still, the quadratic Zeeman effect coupled to the small offset field $B_0 = 1\,\mathrm{mG}$ and a magnetic field gradient ∇B induce an acceleration [66, 67]. Since the coefficients for the quadratic Zeeman effect are different for the two isotopes, a differential acceleration signal results. This also impedes the overlap during the time between release from the optical trap and the delta kick and requires on magnetic field gradients below $3\,\mu\mathrm{G\,m^{-1}}$. That external fields can be sufficiently supressed is shown in [68].

Effective wave front curvature When the atomic ensembles expand in the time interval between two successive interactions with a curved effective beam splitter wave front a phase shift appears [69]. This effect is suppressed in the differential signal because of the similar expansion rates of the two ensembles. In Table 4 the curvature of the retro reflector is assumed to be $R = 250\,\mathrm{km}$ and the resulting effective wave front for an initial collimation of the beam splitter telescope $400\,\mathrm{m}$. By matching the expansion rates, the requirements on R will be reduced to be compatible with a retro reflection mirror surface planarity of $\lambda/50$.

Mean field Even in the regime of linear expansion there is a residual contribution from the mean field energy. This appears in the interferometer signal if the beam splitting at the first pulse is not perfect [70]. To mitigate this effect, the mean ratio between the two isotope populations will be tuned to $N_{87}/N_{85} \approx 1.697(\pm 0.001)$. Thus, negative

Error source	Limit $(10^{-15}\,\mathrm{m\,s^{-2}})$	Conditions
Gravity gradient[1]	2.6	$\Delta z = 1.1 \cdot 10^{-9}\,\mathrm{m}$
	3.5	$\Delta v_z = 3.1 \cdot 10^{-10}\,\mathrm{m}$
Coriolis acceleration	0.62	$\Delta v_x = 3.1 \cdot 10^{-10}\,\mathrm{m}$
	0.62	$\Delta v_y = 3.1 \cdot 10^{-10}\,\mathrm{m}$
Additional overlap dependent terms	0.055	$\Delta x = 1.1 \cdot 10^{-9}\,\mathrm{m}$
	0.0016	$\Delta y = 1.1 \cdot 10^{-9}\,\mathrm{m}$
Others	0.046	
Photon recoil	0.039	Earth's 2nd order gravity gradient
Self-gravity[2]	1	
Static magnetic fields[3]	1	$B_0 = 1\,\mathrm{mG}, \nabla B_0 = 1\,\mathrm{\mu G\,m^{-1}}$
Effective wave front curvature[4]	0.63	Mirror curvature
	0.28	$R = 250\,\mathrm{km}$, initial collimation $\approx 400\,\mathrm{m}$ $T_{at} \approx 0.07\,\mathrm{nK}$
Mean field	2	Beam splitter accuracy $0.1\,\%$ $N_{87}/N_{85} \approx 1.697(\pm 0.001)$
Spurious accelerations	1	Suppression ratio $2.5 \cdot 10^{-9}$, spurious acceleration $4 \cdot 10^{-7}\,\mathrm{m\,s^{-2}}$
Detection efficiency[5]	< 1	$|\epsilon - 1| < 0.003$
Total diff. acceleration	7.9	

Table 4. Preliminary error budget for the STE-QUEST AI
The differential acceleration of $7.9 \cdot 10^{-15}\,\mathrm{m\,s^{-2}}$ was evaluated at perigee for an altitude of $700\,\mathrm{km}$ implying a gravity gradient of $2.2 \cdot 10^{-6}\,\mathrm{s^{-2}}$ and a projection of the local gravitational acceleration of $8\,\mathrm{m\,s^{-2}}$. Dividing the differential acceleration by the projection of local gravitational acceleration leads to the Eötvös ratio. Terms dependent on the overlap and effective wave front curvature were treated as correlated within their subset, while other terms are expected to be uncorrelated. [1] Connected to magnetic field gradient and distance to the center of mass. [2] Calibration during apogee. [3] Relieved by input state reversal. [4] Relaxed by expansion rate match. [5] Post correction from Bayesian fit.

energy shift due to ^{85}Rb intra species interactions and positive energy shifts due to inter species and ^{87}Rb intra species interactions nearly cancel with a remaining uncertainty of $2 \cdot 10^{-15}\,\mathrm{m\,s^{-2}}$.

Detection efficiency   Vibrations will wash out the fringe visibility, but the differential signal can still be extracted from an ellipse fitting technique [71, 72]. If the outputs of the two atom interferometers are not balanced by a factor ϵ, this will be misinterpreted as an acceleration signal. The parameter ϵ can be estimated within parts per thousand contributing an error below $10^{-15}\,\mathrm{m\,s^{-2}}$.

Result The estimated statistical errors compatible with a shot noise limited measurement are stated in Table 3. An overview of the bias errors assessed at perigee for an altitude of 700 km is given in Table 4. Herein, the differential acceleration of $7.9 \cdot 10^{-15}\,\mathrm{m\,s^{-2}}$ has to be divided by the projection of local $g \approx 8\,\mathrm{m\,s^2}$ which leads to an error in the Eötvös ratio of $1 \cdot 10^{-15}$. During the arc at perigee, the projection of the Earth's gravity gradient and local gravitational acceleration change implying an increase in the uncertainty to $2 \cdot 10^{-15}$ at the edges. The maximum perigee altitude of 2200 km and the corresponding arc inhibit the same uncertainty figures.

A crucial point to stay within error budget is the initial overlap and differential velocity. The specified gravity gradient, rotation rates, and magnetic field gradients which could cause a displacement in the optical trap combined with a distance to the satellite's center of mass below 2 m are compatible with the performance budget presented in Table 4. To verify the requirements on relative positioning and velocity of the atomic samples, several images of the atomic ensembles will be taken during the apogee phase with an alternating time of flight of 1 s and 10 s after the Raman kick. Fitting the images will reveal the differential center of mass positions. Averaging over a sufficient number of cycles will then allow a verification at the required precision.

5. Payload

The STE-QUEST atom interferometer payload is subdivided into three main functional units: (i) physics package (PP), laser system (LS) and (iii) electronics as shown in the functional diagram given in Figure 5. The overall preliminary budgets concerning volume, mass and power are detailed in Table 5. Furthermore, a telemetry budget of 110 kbps is allocated to the AI. The instrument design is based on current state-of-the-art cold atom experiments under microgravity, namely the German funded QUANTUS (QUANTengase Unter Schwerelosigkeit) and MAIUS (MAteriewelleninterferometrie Unter Schwerelosigkeit) projects operated in drop tower experiments and the French funded I.C.E. (Intérférométrie Cohéhente pour l'Espace) project operated in zero-g parabola flights.

	Volumes	Volume (l)	Mass (kg)	Average power (W)	Peak power (W)
Physics Package	1 cylinder	342	135	74	157
Laser System	3 boxes	59	52	103	114
Electronics	5 boxes	68	34	431	549
Total			221	608	820

Table 5. Preliminary budget table of the STE-QUEST atom interferometer payload detailing volume, mass and power for the three functional units. All numbers for mass and power include a 20% component level margin but no system level margin.

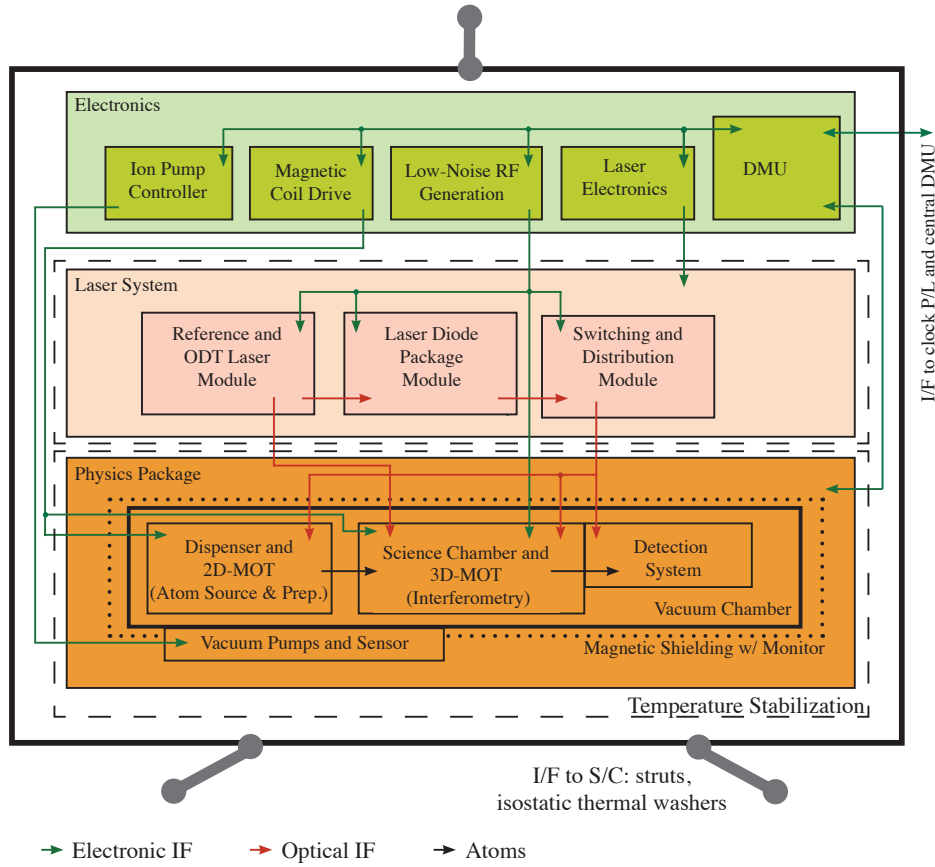The Physics Package comprises the Titanium made vacuum chamber for cold

Figure 5. Functional diagram of the STE-QUEST atom interferometer payload. It consists of physics package (PP), laser system (LS) and electronics with given subsystems and interfaces.

atom preparation and manipulation including atom source, ultra-high vacuum science chamber, detection unit, vacuum pump system and Mu-metal magnetic shielding. The science chamber houses the three layer atom chip and features a dodecagon design providing the optical accesses for optical dipole trap (ODT), 3D-MOT, interferometry, fluorescence and absorption detection and Raman kick beams. The atom source consists of a heated Rb reservoir and a 2D-MOT which is attached to the science chamber using diffusion brazing. The homogeneous magnetic offset fields are generated using three pairs of coils in Helmholtz configuration. A four layer Mu-metal shielding with a suppression factor > 10.000 is foreseen around the physics package in order to suppress external magnetic stray fields. The shielding also has to withstand internal magentic field up to 160 G (Feshbach field) without permanent damage. The pump system needs to maintain an ultra-high vacuum at the 10^{-11} mbar level and uses a combination of an ion getter pump and a passive getter pump.

The Laser System is housed in three boxes: (i) a Telecom fiber technology based reference and optical dipole trap laser module, (ii) a micro-integrated, high-power 780 nm laser diode package module for atom manipulation, cooling and detection and (iii) a switching and distribution module delivering the laser beams according to the

experimental sequence (cf. chapter 3) to the physics package. The switching module is based on Zerodur bonding technology and uses a combination of acousto-optic modulators (AOMs) for fast switching and mechanical shutters for highest extinction ratio, while the distribution module is realized as an optical fiber technology beam splitter array.

The AI instrument electronics includes a data management unit (DMU) which controls all other electronics units and the overall payload, including housekeeping data gathering, a magnetic coil drive unit providing the low noise current drivers for magnetic field generation, a low-noise RF generation generating the $6.8\,\mathrm{GHz}$ and $3\,\mathrm{GHz}$ signals corresponding to the hyperfine transitions in ^{87}Rb and ^{85}Rb, respectively and the signals for RF knife and driving electro-optical components, a laser control unit providing the low noise current supplies and temperature controls for the lasers, and an ion pump controller delivering the high voltage power supply for the ion getter pump.

6. Conclusion

The STE-QUEST mission aims to perform a quantum test of the Universality of Free Fall using cold atom interferometry with unprecedented precision, exploring in this way the frontiers of the validity of General Relativity. The mission will track the propagation of two matter waves of atomic species, i.e. two Bose Einstein condensates consisting of ^{85}Rb and ^{87}Rb, which fall freely in Earth's gravitational field. The goal of the mission is to reach an accuracy of $\eta \leq 2 \cdot 10^{-15}$ over the entire mission period, improving the best test performed on Earth so far by at least two orders of magnitude. With this accuracy a new window is opened to find experimental evidence of a quantum theory of gravity – today's main open question in theoretical physics.

References

[1] C. M. Will, The confrontation between general relativity and experiment, Liv. Rev. Rel. **9**, 3 (2006).

[2] C. Lämmerzahl, Testing basic laws of gravitation - Are our postulates on dynamics and gravitation supported by experimental evidence?, in *Mass and Motion in General Relativity*, edited by L. Blanchet, A. Spallici, and B. Whiting Vol. 162, p. 25, Berlin, 2011, Springer Verlag.

[3] S. Liberati, Tests of Lorentz invariance: A 2013 update, Class. Quant. Grav. **30**, 133001 (2013).

[4] C. Kiefer, *Quantum Gravity*, 3rd ed. (Oxford University Press, 2012).

[5] T. Damour and A. M. Polyakov, The string dilaton and a least coupling principle, Nucl. Phys. B **423**, 532 (1994).

[6] T. Damour, F. Piazza, and G. Veneziano, Runaway dilaton and equivalence principle violations, Phys. Rev. Lett. **89**, 081601 (2002).

[7] T. Damour, Theoretical aspects of the equivalence principle, Class. Quant. Grav. **29**, 184001 (2012).

[8] E. Fischbach *et al.*, Reanalysis of the Eötvös experiment, Phys. Rev. Lett. **56**, 3 (1986).

[9] E. Fischbach and C. Talmadge, *The Search for Non-Newtonian Gravity* (Springer, New York, U.S.A., 1998).

[10] C. Brans and R. H. Dicke, Mach's principle and a relativistic theory of gravitation, Phys. Rev. **124**, 925 (1961).

[11] G. Dvali and M. Zaldarriaga, Changing α with time: Implications for fifth-force-type experiments and quintessence, Phys. Rev. Lett. **88**, 091303 (2002).

[12] D. Puetzfeld and Y. N. Obukhov, Covariant equations of motion for test bodies in gravitational theories with general nonminimal coupling, Phys. Rev. D **87**, 044045 (2013).

[13] S. M. Carroll, S. Mantry, and M. J. Ramsey-Musolf, Implications of a scalar dark force for terrestrial experiments, Phys. Rev. D **81**, 063507 (2010).

[14] C. Wetterich, Crossover quintessence and cosmological history of fundamental "constants", Phys. Lett. B **561**, 10 (2003).

[15] J. Chen, *Probing scalar couplings through tests of the equivalence principle*, PhD thesis, The University of Chicago, Illinois, USA, 2005.

[16] C. Will, *Theory and Experiment in Gravitational Physics*, 2nd ed. (Cambridge University Press, Cambridge; New York, 1993).

[17] D. Colladay and V. Kostelecký, Lorentz-violating extension of the standard model, Phys. Rev. D **58**, 116002 (1998).

[18] J. C. LoPresto, C. Schrader, and A. Pierce, Solar gravitational redshift from the infrared oxygen triplet, Astrophys. J. **376**, 757 (1991).

[19] T. P. Krisher, D. D. Morabito, and J. D. Anderson, The Galileo solar redshift experiment, Phys. Rev. Lett. **70**, 2213 (1993).

[20] R. F. C. Vessot *et al.*, Test of relativistic gravitation with a space-borne hydrogen maser, Phys. Rev. Lett. **45**, 2081 (1980).

[21] G. Hechenblaikner *et al.*, STE-QUEST mission and system design - Overview after completion of phase-A, arXiv:1310.0084 [physics.ins-det] (2013).

[22] G. M. Tino *et al.*, Precision gravity tests with atom interferometry in space, Nucl. Phys. B (Proc. Suppl.) **243**, 203 (2013).

[23] S. Schlamminger *et al.*, Test of the equivalence principle using a rotating torsion balance, Phys. Rev. Lett. **100**, 041101 (2008).

[24] J. G. Williams, S. G. Turyshev, and D. H. Boggs, Lunar laser ranging tests of the equivalence principle, Class. Quant. Grav. **29**, 184004 (2012).

[25] A. Peters, K. Y. Chung, and S. Chu, Measurement of gravitational acceleration by dropping atoms, Nature **400**, 849 (1999).

[26] S. Fray *et al.*, Atomic interferometer with amplitude gratings of light and its applications to atom based tests of the equivalence principle, Phys. Rev. Lett. **93**, 240404 (2004).

[27] A. Bonnin *et al.*, Simultaneous dual-species matter-wave accelerometer, Phys. Rev. A **88**, 043615 (2013).

[28] G. M. Tino, Testing gravity with atom interferometry, Lecture II in "E. Fermi" School on *Atom Interferometry*, Varenna, 2013.

[29] Homepage of the project: http://www.iqo.uni-hannover.de/atlas.html.

[30] P. Hamilton *et al.*, Progress towards a test of the universality of free fall using a ^{6}Li-^{7}Li atom interferometer, in *APS Division of Atomic, Molecular and Optical Physics Meeting Abstracts*, p. 5004, 2012.

[31] S. Dimopoulos *et al.*, Testing general relativity with atom interferometry, Phys. Rev. Lett. **98**, 111102 (2007).

[32] F. Sorrentino *et al.*, A compact atom interferometer for future space missions, Micrograv. Sci. Technol. **22**, 551 (2010).

[33] G. Varoquaux *et al.*, How to estimate the differential acceleration in a two-species atom interferometer to test the equivalence principle, New J. Phys. **11**, 113010 (2009).

[34] J. Rudolph *et al.*, Degenerate quantum gases in microgravity, Micrograv. Sci. Technol. **23**, 287 (2011).

[35] P. Touboul *et al.*, The microscope experiment, ready for the in-orbit test of the equivalence principle, Class. Quant. Grav. **29**, 184010 (2012).

[36] J. Overduin *et al.*, STEP and fundamental physics, Class. Quant. Grav. **29**, 184012 (2012).

[37] A. M. Nobili *et al.*, 'Galileo Galilei' (GG): space test of the weak equivalence principle to 10^{-17} and laboratory demonstrations, Class. Quant. Grav. **29**, 184011 (2012).

[38] H. Müntinga *et al.*, Interferometry with bose-einstein condensates in microgravity, Phys. Rev. Lett. **110**, 093602 (2013).

[39] D. Giulini and A. Groardt, The Schrödinger-Newton equation as a non-relativistic limit of self-gravitating Klein-Gordon and Dirac fields, Class. and Quant. Grav. **29**, 215010 (2012).

[40] L. Cacciapuoti, STE-QUEST Science Requirements Document, FPM-SA-DC-00001, issue 1, revision 5 (April 2013), *Technical report*, European Space Agency, available at http://sci.esa.int/ste-quest/, 2013.

[41] S. M. Dickerson *et al.*, Multiaxis inertial sensing with long-time point source atom interferometry, Phys. Rev. Lett. **111**, 083001 (2013).

[42] J. M. Hogan, D. M. S. Johnson, and M. A. Kasevich, Light-pulse atom interferometry, in *Atom Optics and Space Physics*, edited by E. Arimondo *et al.*, p. 411, 2009.

[43] P. Cladé *et al.*, Theoretical analysis of a large momentum beamsplitter using Bloch oscillations, Eur. Phys. J. D **59**, 349 (2010).

[44] S. Chu *et al.*, Proposal for optically cooling atoms to temperatures of the order of 10 to the -6th K, Opt. Lett. **11**, 73 (1986).

[45] H. Ammann and N. Christensen, Delta kick cooling: A new method for cooling atoms, Physical Review Letters **78**, 2088 (1997).

[46] M. Morinaga *et al.*, Manipulation of motional quantum states of neutral atoms, Phys. Rev. Lett. **83**, 4037 (1999).

[47] T. Lévèque *et al.*, Enhancing the area of a Raman atom interferometer using a versatile double-diffraction technique, Phys. Rev. Lett. **103**, 080405 (2009).

[48] G. Tackmann *et al.*, Self alignment of a compact large-area atomic Sagnac interferometer, New J. Phys. **14**, 015002 (2012).

[49] W. Hänsel *et al.*, Bose-Einstein condensation on a microelectronic chip, Nature **413**, 498 (2001).

[50] R. Folman *et al.*, Adv. At. Mol. Opt. Phys. **48**, 263 (2002).

[51] J. Fortágh and C. Zimmermann, Magnetic microtraps for ultracold atoms, Rev. Mod. Phys. **79**, 235 (2007).

[52] K. Posso-Trujillo *et al*, Compact strongly interacting quantum mixtures for precision atom interferometry, in preparation (2013).

[53] K. Dieckmann *et al.*, Two-dimensional magneto-optical trap as a source of slow atoms, Phys. Rev A **58**, 3891 (1998).

[54] T. van Zoest *et al.*, Bose-Einstein Condensation in Microgravity, Science **328**, 1540 (2010).

[55] J. Reichel, W. Hänsel, and T. W. Hänsch, Atomic micromanipulation with magnetic surface traps, Phys. Rev. Lett. **83**, 3398 (1999).

[56] S. B. Papp, J. M. Pino, and C. E. Wieman, Tunable Miscibility in a Dual-Species Bose-Einstein Condensate, Phys. Rev. Lett. **101**, 040402 (2008).

[57] P. A. Altin *et al.*, 85Rb tunable-interaction Bose-Einstein condensate machine, Rev. Sci. Instrum. **81**, 063103 (2010).

[58] J.-F. Clément *et al.*, All-optical runaway evaporation to Bose-Einstein condensation, Phys. Rev. A **79**, 061406 (2009).

[59] A. Roura, W. Zeller, and W. P. Schleich, Overcoming loss of contrast in atom interferometry due to gravity gradients, in preparation.

[60]

[61] P. Cheinet *et al.*, Measurement of the sensitivity function in a time-domain atomic interferometer, IEEE Trans. Instrum. Meas. **57**, 1141 (2008).

[62] S.-Y. Lan *et al.*, Influence of the Coriolis force in atom interferometry, Phys. Rev. Lett. **108**, 090402 (2012).

[63] J. M. McGuirk *et al.*, Sensitive absolute-gravity gradiometry using atom interferometry, Phys. Rev. A **65**, 033608 (2002).

[64] J. Le Gouët *et al.*, Influence of lasers propagation delay on the sensitivity of atom interferometers, Eur. Phys. J. D. **44**, 419 (2007).

[65] K. Bongs, R. Launay, and M. A. Kasevich, High-order inertial phase shifts for time-domain atom interferometers, Appl. Phys. B **84**, 599 (2006).

[66] J. Le Gouët *et al.*, Limits to the sensitivity of a low noise compact atomic gravimeter, Appl. Phys. B **92**, 133 (2008).

[67] D. A. Steck, Rubidium 87 D line data, revision 2.1, Online, 2008, http://steck.us/alkalidata/rubidium87numbers.pdf.

[68] A. Milke *et al.*, Atom interferometry in space: Thermal management and magnetic shielding, in preparation.

[69] A. Louchet-Chauvet *et al.*, The influence of transverse motion within an atomic gravimeter, New J. Phys. **13**, 065025 (2011).

[70] J. E. Debs *et al.*, Cold-atom gravimetry with a Bose-Einstein condensate, Phys. Rev. A. **84**, 033610 (2011).

[71] G. T. Foster *et al.*, Method of phase extraction between coupled atom interferometers using ellipse-specific fitting, Opt. Lett. **27**, 951 (2002).

[72] J. K. Stockton, X. Wu, and M. A. Kasevich, Bayesian estimation of differential interferometer phase, Phys. Rev. A **76**, 33613 (2007).